Nano Research

Open Access

Research Article

Triple modification engineering to enhance structural stability and ionic-electronic transport kinetics of lithium-rich manganese-based cathode materials

Xingpeng Cai[1], Shiyou Li[1,2,3], Ningshuang Zhang[1,2,3], Jiawen Zhang[1], Jingxuan Yan[1], and Xiaoling Cui[1,2,3] ✉

[1] *School of Petrochemical Technology, Lanzhou University of Technology, Lanzhou 730050, China*
[2] *Key Laboratory of Low Carbon Energy and Chemical Engineering of Gansu Province, Lanzhou 730050, China*
[3] *Engineering Research Center of Cathode Material for Lithium-ion Battery of Gansu Province, Baiyin 730900, China*

Cite this article: *Nano Research*, **2025**, *18*, 94907813. https://doi.org/10.26599/NR.2025.94907813

ABSTRACT: The development of strategies to inhibit structural degradation and surface side reactions is the key to promoting the large-scale application of lithium-rich manganese-based cathode materials $Li_{1.2}Mn_{0.54}Ni_{0.13}Co_{0.13}O_2$ (LMNCO). Herein, LMNCO was triply modified from the inside to the outside, by bulk doping of Mo^{6+}, fabricating oxygen vacancies (OVs) defects, and surface coating of S, N-doped carbon nanolayers (SNCN). The integration of Mo^{6+} doping and OVs defects widens and stabilizes the Li^+ diffusion channel, and the surface coating of SNCN provides additional electrons for LMNCO in the conduction band region, achieving a simultaneous improvement in both ionic and electronic conductivity. Meanwhile, Mo^{6+} doping and OVs mitigate the irreversible phase transitions caused by oxygen loss and transition metal (TM) out-of-plane migration, while SNCN inhibits the corrosion of the electrolyte on the material surface and enhances the stability of the surface structure. Benefiting from the synergistic effect of these modifications, the structural evolution of the modified material is highly reversible, and the layered structure remains intact during repeated lithiation/delithiation processes, while the mechanical properties of material are also improved, effectively suppressing crack generation and TM dissolution. As a result, at room temperature (25 °C), the modified cathode demonstrates a high capacity retention of 94.6% after 200 cycles at 1 C, and a high rate capacity of 161.0 mAh·g^{-1} at 5 C. Especially, under harsh conditions, the capacity retention is 76.3% after 150 cycles at 55 °C and 1 C. This work provides a new solution for developing advanced LMNCO cathode materials.

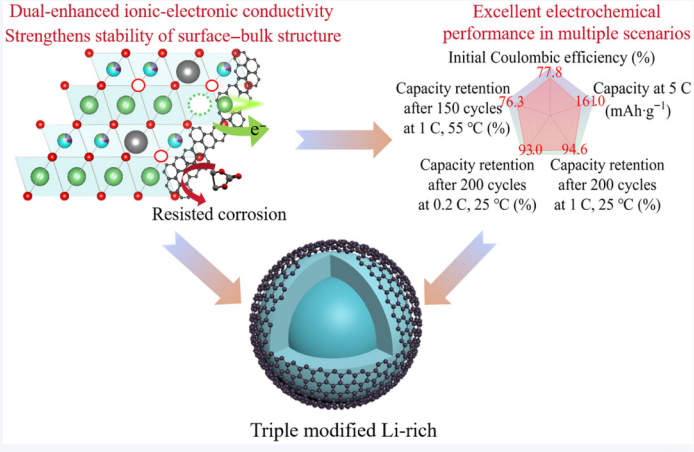

KEYWORDS: cathode materials, lithium-rich manganese-based layered oxides, oxygen vacancies, Mo^{6+} doping, S, N-doped carbon nanolayers

1 Introduction

The development of cathode materials with low cost and high energy density represents a significant avenue for the accelerated evolution of lithium-ion batteries (LIBs) in the domain of power vehicles and energy storage devices [1, 2]. The lithium-rich manganese-based cathode materials $Li_{1.2}Mn_{0.54}Ni_{0.13}Co_{0.13}O_2$ (LMNCO) achieve a high specific capacity of > 300 mAh·g^{-1} by their unique anionic/cationic joint involvement in the redox mechanism [3–5]. Besides, abundant Mn reserves on Earth help reduce the cost of LMNCO. However, LMNCO is still hampered by several problems in practical applications, including low initial Coulombic efficiency (ICE), serious capacity/voltage decay, and poor rate performance [6]. This is because, in order to obtain a higher specific capacity, LMNCO typically triggers anionic redox reactions at high voltage, which causes significant Li removal and oxygen loss. Meanwhile, transition metal (TM) is prone to out-of-plane migration towards the Li layer during cycling, driving an

Received: May 23, 2025; **Revised:** July 15, 2025
Accepted: July 17, 2025

✉Address correspondence to xlcuilw@163.com

irreversible phase transition from layered structure to spinel and rock salt structures [7, 8]. In addition, conventional carbonate-based electrolytes will cause uncontrolled side reactions with LMNCO surfaces at high voltage, accelerating TM dissolution and particle degradation (Fig. 1(a)) [9, 10].

To mitigate structural degradation, doping strategies that can effectively block the TM migration path and stabilize the lattice oxygen have been reported many times. The doping elements usually have two selective criteria, namely, no redox activity and strong TM–O binding energy. Correspondingly, Sb [11], Al [12], Ta [13], Nb [14], and Zr [15] all show good modification effects. Recently, we have found that high-valence-state Mo^{6+} doping contributes to reducing the Coulomb repulsion among the three unpaired electrons in t_{2g} orbitals of Mn^{4+}, and promoting the strength of covalent Mn^{4+}–O^{2-} bond, thereby strengthening the stability of the main structural framework, and mitigating the structural collapse as well as the irreversible phase transition in the deep delithiation state [16]. Although these doping strategies have alleviated the structural instability, they could not effectively inhibit the corrosion of the electrolyte on the active material surface (Fig. 1(b)). That is, it is difficult for a single modification strategy to both improve the structural stability of the surface and the bulk.

To inhibit the electrochemical decay of LMNCO caused by both internal reactions and external factors, the doping and coating synergistic modification strategy has been reported. Generally, the coating materials are mainly focused on metal oxides [17], fast ion conductors [18], carbon materials [19], and fluorides [20]. Among them, carbon coating has attracted the most attention, owing to its excellent conductivity and flexibility. It can not only effectively improve the electron transport rate of LMNCO but also mitigate surface side reactions and volume changes of particles during cycling. For instance, synergistic strategy of B^{3+} doping and carbon coating has enhanced the electronic conductivity of the materials, reduced the internal resistance of the batteries, and resisted erosion by electrolytes, thereby improving the structural and cycling stability of materials [21]. Likewise, synergistic strategy of bulk K^+ doping and amorphous carbon coating has proved to be helpful in stabilizing the lattice oxygen and restraining the structural distortion in LMNCO, thereby effectively suppressing changes in lattice parameters and the formation of microcracks during cycling [22]. However, the lack of strong covalent bonding between the carbon coating and the host material may lead to coating cracking and detachment in the long cycle process, thereby accelerating capacity decay. Thus, the introduction of anion defects into the carbon coating has come into view [23]. It can not only strengthen the strong coupling effect between anions and TM in the LMNCO

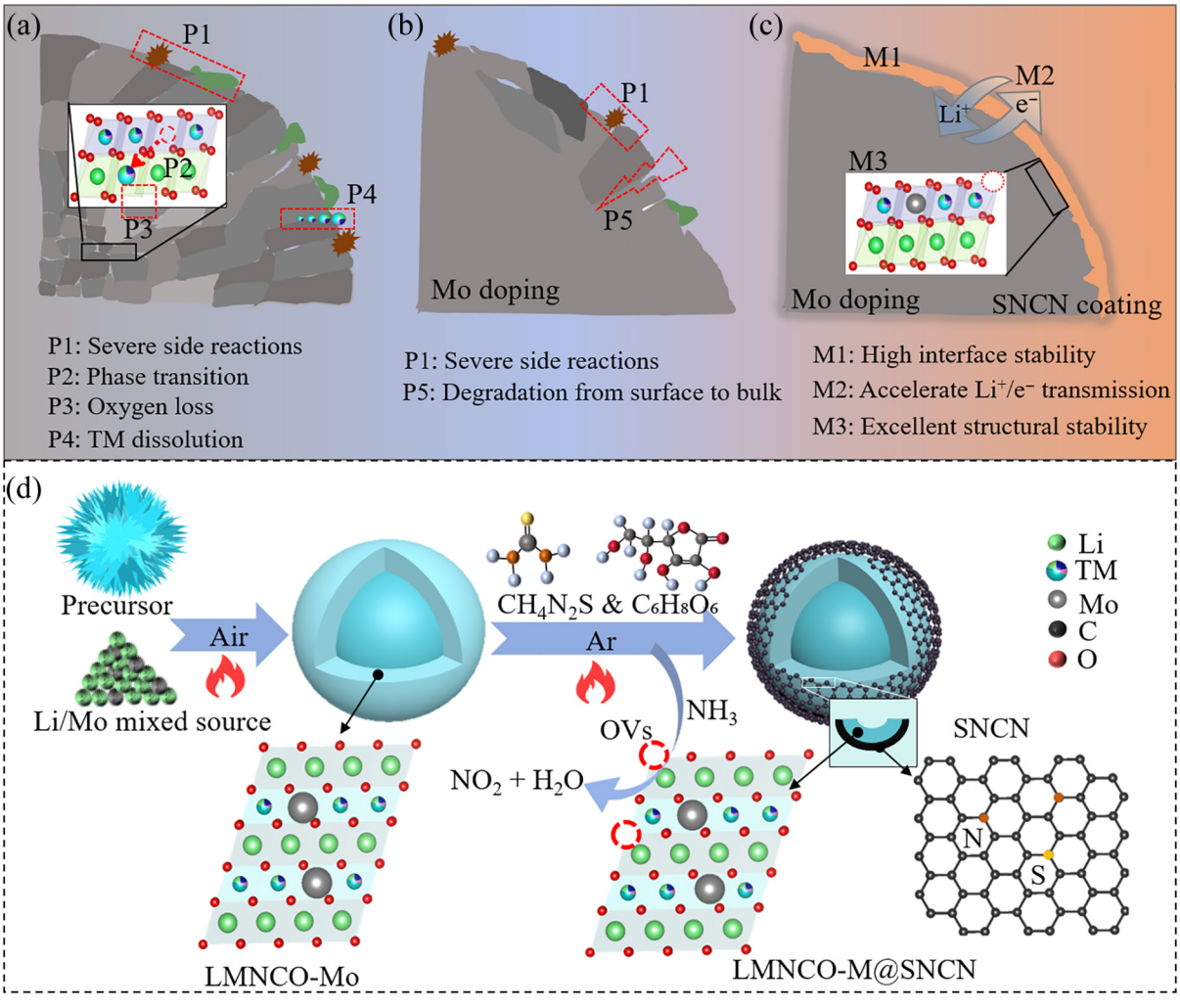

Figure 1 ((a) and (b)) Degradation schematics of (a) pristine LMNCO and (b) Mo doping LMNCO. ((c) and (d)) Modification and synthesis schematics of LMNCO-M@SNCN.

but also improve the pore structure, thereby enhancing the electronic conductivity and cycling stability of the carbon coating.

Although the doping and coating synergistic modification strategy improves the performance of the LMNCO significantly, performance degradation still occurs under harsh conditions (such as high temperature and high rates), due to the serious surface oxygen loss. Current research indicates that increasing the concentration of oxygen vacancies (OVs) on the LMNCO surface to reduce the coupling of O–O dimers is one of the most effective strategies for suppressing oxygen loss under extreme conditions [24]. That is, developing a strategy that can face the three challenges of stabilizing the bulk–surface structure, enhancing the coupling between the coating and active materials, and suppressing irreversible oxygen loss under harsh conditions is crucial for accelerating the large-scale application of LMNCO.

Herein, LMNCO is triply modified from the inside to the outside, by bulk Mo^{6+} doping, fabricating OVs defects, and surface coating of S, N-doped carbon nanolayers (SNCN). During pyrolysis, the reduction properties of CH_4N_2S and $C_6H_8O_6$ facilitate the formation of OVs and increase the content of Mn^{3+}. More than that, the abundant S/N co-doped defects in SNCN enhance the connection with LMNCO. The results indicate that the SNCN provides additional electrons for the LMNCO in the conduction band region, while Mo^{6+} doping and OVs widen and stabilize the Li^+ diffusion channel, achieving a simultaneous improvement in ionic and electronic conductivity. As a result, the modified material effectively mitigates the oxygen loss and irreversible phase transition, inhibits the corrosion of active materials by adverse interfacial reactions, and thus ensures excellent structural and mechanical stability during cycling process (Fig. 1(c)). This work provides a new direction for advanced LMNCO, which helps to break the bottleneck of commercial application.

2 Methods

2.1 Material synthesis

The pristine LMNCO was synthesized via the precipitation method. Firstly, $Mn(CH_3COO)_2{\cdot}4H_2O$, $Ni(CH_3COO)_2{\cdot}4H_2O$, and $Co(CH_3COO)_2{\cdot}4H_2O$ were dissolved fully in deionized water according to the stoichiometric ratio to form a mixed metal solution. At 75 °C, the precipitant consisting of a mixture of Na_2CO_3 and NaOH was slowly dripped into the mixed metal solution until pH = 8. Then, the precipitation was calcined in a muffle furnace at 450 °C for 5 h to obtain the precursor. After thorough mixing with $CH_3COOLi{\cdot}2H_2O$, the precursor was calcined at 900 °C for 12 h to obtain the pristine LMNCO. Similarly, $Li_{1.2}Mn_{0.53}Ni_{0.13}Co_{0.13}Mo_{0.01}O_2$ (LMNCO-M) was synthesized with the addition of $(NH_4)_6Mo_7O_{24}{\cdot}4H_2O$. The synthesis of LMNCO-M@SNCN (LMNCO-M@SNCN) was achieved by dispersing the as-prepared LMNCO-M in a mixed solution composed of CH_4N_2S (2 wt.%) and $C_6H_8O_6$ (1 wt.%), followed by heating at 400 °C for 3 h under Ar atmosphere. The synthesis and modification schematic is given in Fig. 1(d).

2.2 Electrochemical measurements

The electrochemical tests were performed on CR2025 coin cells. To obtain the working cathode, the active material, carbon black and polyvinylidene fluoride (PVDF) were uniformly mixed in N-methyl-1,2-pyrrolidone with the ratio of 80 wt.%:10 wt.%:10 wt.%, followed by coating on an aluminium foil and then dried at 110 °C. In the coin cells, 1 M $LiPF_6$ in ethyl carbonate/diethylene carbonate (EC/DEC, 1:1 in volume) and metal Li were used as electrolyte and anode, respectively. Cycle performance, rate capability, and galvanostatic intermittent titration technique (GITT, galvanostatic charging/discharging and settling times were 10 and 30 min, respectively) were performed on the Land test system (CT2001A, Wuhan). The leakage current was tested by a DH7006B electrochemical workstation (Dong Hua, Jiangsu) by initially charging the sample to 4.8 V at a 0.1 C rate, followed by holding at 4.8 V for 3 h while monitoring the current variation. The potential resolved *in-situ* electrochemical impedance spectroscopy (PRIs-EIS) was tested by a CHI660E electrochemical workstation (CH instruments Inc., China), by recording the change of EIS with the voltammetric scanning process, from the open-circuit voltage to 4.8 V, with a jump amplitude of 5 mV, in the frequency range of 0.01 Hz–100 kHz.

2.3 Material characterizations

The crystal structure was characterized by X-ray diffraction (XRD, Rigaku Smart Lab) in 2θ range of 10° to 90° with a scanning rate of 2 °·min^{-1}. The XRD Rietveld refinements were carried out using the software of General Structure Analysis System 2 (GASA2). The morphology and elemental distribution of samples were identified by scanning electron microscopy (SEM, CIQTEK Co., Ltd. FESEM5000) and energy dispersive X-ray spectrometry (EDS). The microstructure of samples was acquired by high-resolution transmission electron microscopy (HRTEM, JEOL JEM-F200 type). The OVs of samples were identified by electron paramagnetic resonance (EPR, Bruker E500 type). The elemental composition and valence state were identified by X-ray photoelectron spectroscopy (XPS, Thermo Scientific K-Alpha type). Gas evolution analysis in batteries was performed by differential electrochemical mass spectroscopy (DEMS, Linglu QMG100). The electronic work function and Young's modulus of the samples were measured using an atomic force microscope (AFM, Park NX10). The electronic conductivity of the samples was obtained with four-point probes (RTS-9). The dissolved amounts of metallic elements were detected using inductively coupled plasma optical emission spectroscopy (ICP-OES, Thermo Scientific iCAP PRO).

2.4 Density functional theory (DFT) calculations

DFT calculations were performed in MedeA software using the Vienna *ab-initio* simulation package (VASP), adopting the projector-augmented wave (PAW) approach. To treat the exchange-correlation effects, the generalized gradient approximation (GGA) with Perdew–Burke–Ernzerhof (PBE) function was obtained. The TM electronic structure was corrected using the GGA + Hubbard parameter (U) method, and the U value for the Mn 3d state was 4.0 eV. The plane-wave cutoff energy for each structure was 520 eV, and the convergence criteria for energy and force were 1×10^{-5} eV and 0.02 eV·Å^{-1}, respectively.

3 Results and discussion

The Rietveld refinement of XRD patterns of LMNCO-M@SNCN and LMNCO are shown in Fig. 2(a) and Fig. S1(a) in the Electronic Supplementary Material (ESM). The sharp diffraction peaks of both samples precisely match the hexagonal a-$NaFeO_2$ structure (space group: $R\bar{3}m$). The weak peaks in the range of 20°–23° correspond

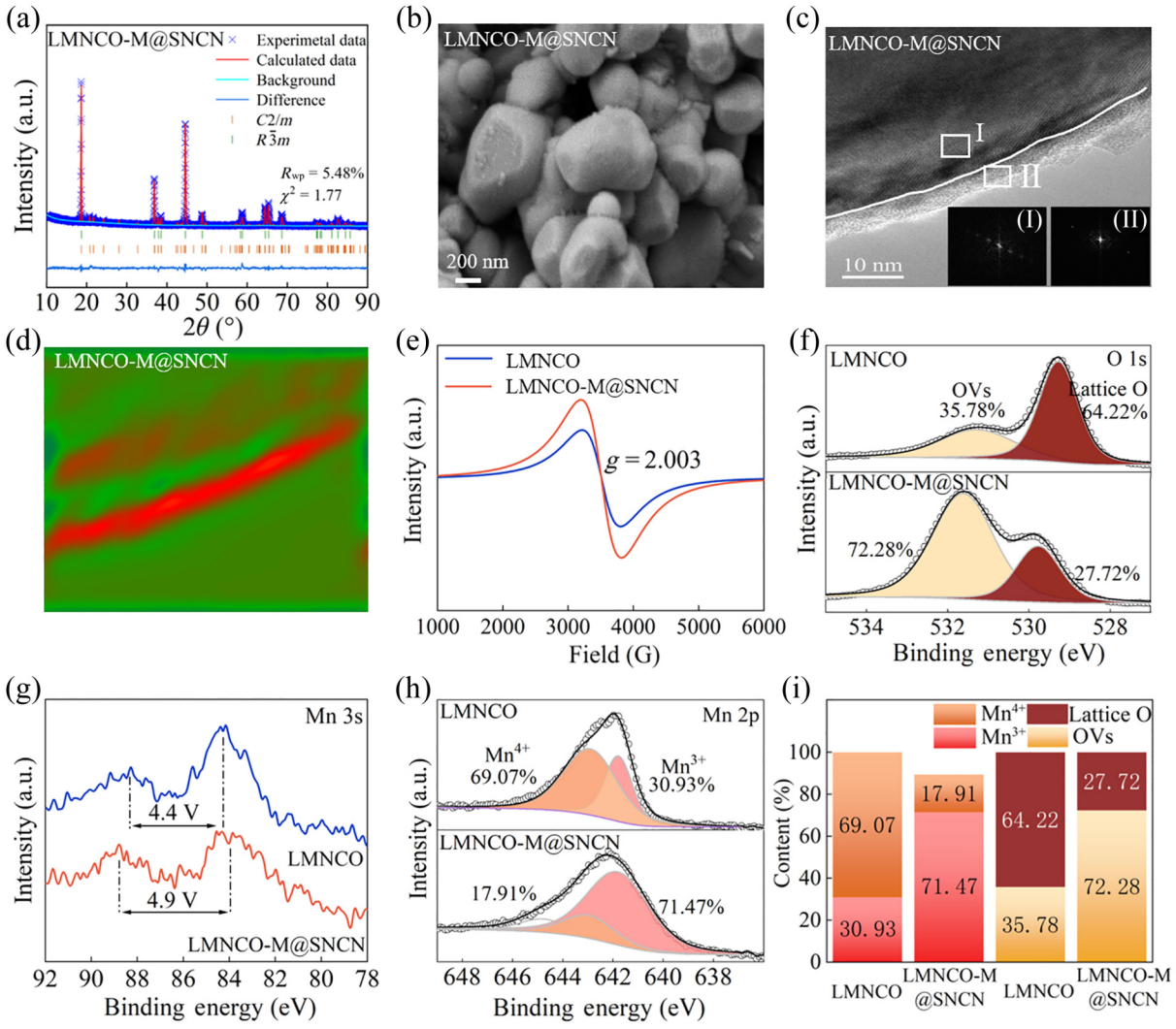

Figure 2 (a) Rietveld analysis of XRD patterns, (b) SEM image, (c) HRTEM image, and (d) GPA image of LMNCO-M@SNCN. (e) EPR spectra of LMNCO and LMNCO-M@SNCN. ((f)–(i)) XPS spectra of (f) O 1s, (g) Mn 3s, (h) Mn 2p, and (i) the statistical graph about the content of Mn^{3+}/Mn^{4+} and lattice O/OVs for LMNCO and LMNCO-M@SNCN.

to the superlattice structure of the Li_2MnO_3 phase (space group: $C2/m$) [25]. The fitting results in Table S1 in the ESM show that the lattice parameters c and V of LMNCO-M@SNCN are slightly increased compared to LMNCO, which is attributed to the occupation of the TM site by Mo^{6+} with larger ionic radius. The widening of the c value facilitates the expansion of Li^+ diffusion channel, resulting in improved rate performance of the electrode and alleviated polarization. Figure 2(b) and Fig. S1(b) in the ESM show the SEM images of the two samples. By comparison, the LMNCO-M@SNCN surface is rougher, suggesting that the products derived from the pyrolysis of CH_4N_2S and $C_6H_8O_6$ are reorganized with the surface of the active materials. Correspondingly, EDS mapping confirms that the elements of C, N, and S are uniformly distributed on the LMNCO-M@SNCN surface after reorganization (Figs. S2(a) and S2(b) in the ESM). Besides, the signals of Mo^{6+} and C forming chemical bonds with N and S were captured by XPS spectra in LMNCO-M@SNCN (Figs. S2(c)–S2(e) in the ESM). Moreover, HRTEM was further applied to analyze the surface structure of LMNCO-M@SNCN. As shown in Fig. 2(c), SNCN coating with a thickness of about 5 nm appears on the LMNCO-M@SNCN surface, and the fast Fourier transform (FFT) images of the coating region (II) are different from that of the bulk region (I), that is, the ordered arrangement of halo dots almost disappeared. Additionally, the smooth and uniform red streaks in the geometric phase angle analysis (GPA) demonstrate that the coating is uniformly wrapped around the particle surface (Fig. 2(d)). The uniform and thin SNCN coating on the LMNCO-M@SNCN surface can improve electrochemical performance by inhibiting electrolyte corrosion and providing excellent conductivity.

The EPR spectra of both samples are shown in Fig. 2(e), and the g-factor of 2.003 is the characteristic response signal of the OVs. Compared with LMNCO, the signal peak of LMNCO-M@SNCN is sharper, indicating enhanced OVs concentration on the modified sample surface. Moreover, the XPS spectra of O 1s further validate this result. As shown in Fig. 2(f), the relative area of the OVs signal peaks (531.6 eV) in LMNCO-M@SNCN increased from 35.78% in LMNCO to 72.28% [26]. We believe that the increase in OVs concentration originates from the gas–solid reaction between NH_3, the decomposition product of CH_4N_2S, and the lattice oxygen on the LMNCO-M@SNCN surface. Besides, in the Mn 3s spectra (Fig. 2(g)), the spacing of the split peaks of the modified sample

increased from 4.4 to 4.9 eV, indicating that the valence state of Mn gradually decreased from +4 to +3 [27]. Subsequently, fitting results of the Mn $2p_{3/2}$ split peak reveal that the relative area of the Mn^{3+} peak increases from 30.93% of LMNCO to 71.47% of LMNCO-M@SNCN (Fig. 2(h)). The increased Mn^{3+} content in LMNCO-M@SNCN is related to the reducing action of CH_4N_2S and $C_6H_8O_6$ at high temperatures. From the above, compared to pristine LMNCO, the modified LMNCO-M@SNCN exhibits higher OVs concentrations and Mn^{3+} content (Fig. 2(i)).

Various electrochemical tests were performed to evaluate the effects of triple modification strategy with Mo^{6+} doping, OVs defects, and SNCN coating layer on the electrochemical performance. Firstly, the initial charge/discharge curves of LMNCO/Li and LMNCO-M@SNCN/Li half-cell are shown in Fig. 3(a). Each sample exhibits the typical redox characteristic of the Li-rich layered oxide. The initial discharge capacity of LMNCO-M@SNCN/Li cell is 268.7 mAh·g^{-1}, significantly higher than that of LMNCO/Li cell (247.2 mAh·g^{-1}). Meanwhile, the ICE increases from 65.6% to 77.8% after triple modification. To clarify the main reasons for the improvement of LMNCO-M@SNCN/Li cells, the interfacial stability and anionic reversibility of both samples were analyzed by leakage current (chronocurrent method) and DEMS tests. In leakage current curves (Fig. S3(a) in the ESM), the lower current density of LMNCO-M@SNCN/Li cell indicates that the side reactions at surface are well suppressed. In DEMS spectra (Fig. S3(b) in the ESM), a significant amount of O_2 is detected in pristine LMNCO, with the peak concentration of 0.0818 μmol·min^{-1}. In contrast, no obvious peak is observed in DEMS spectra of LMNCO-M@SNCN, indicating the suppression of irreversible oxygen loss and resulting in an enhanced reversibility of anions. Therefore, we believe that the increased discharge capacity of LMNCO-M@SNCN originates from the enhanced charge transfer kinetics among active materials by SNCN, and the reduction of active Li^+ loss by mitigating interfacial side reactions. Meanwhile, Mo^{6+} doping and OVs enhance the anion redox reversibility, thereby significantly improving the ICE of LMNCO-M@SNCN.

Figure 3(b) and Fig. S4(a) in the ESM display the cycling performances of both samples within charge/discharge rates of 1 and 0.2 C (1 C = 250 mA·h^{-1}) at the voltage range of 2.0–4.8 V. At each discharge rate, the discharge capacity and cycling stability of LMNCO-M@SNCN are superior to those of LMNCO. For example, LMNCO-M@SNCN/Li cell maintains a discharge capacity of 193.1 mAh·g^{-1} at 1 C after 200 cycles, with a capacity retention rate of 94.6%. This is a significant improvement over

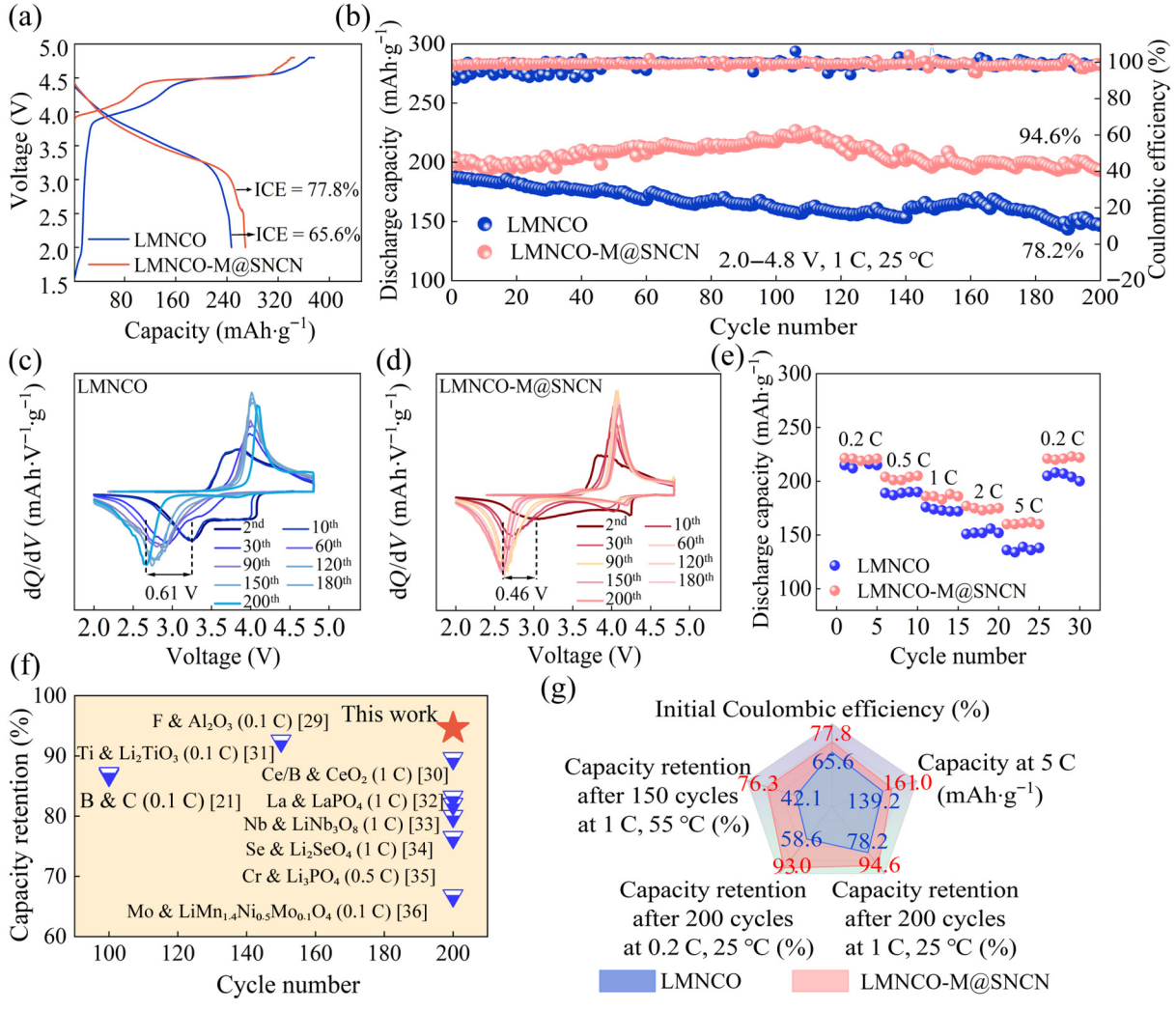

Figure 3 (a) Initial charge–discharge curves, (b) cycling stability at 1 C and 25 °C, ((c) and (d)) dQ/dV curves, and (e) rate performances of LMNCO/Li and LMNCO-M@SNCN/Li cells. (f) Electrochemical performance comparison of triply modified Li-rich materials with those reported in earlier literatures. (g) Electrochemical performance comparison between LMNCO/Li and LMNCO-M@SNCN/Li cells in the form of radar image.

LMNCO/Li cell, which has capacity retention rate of only 78.2%. As shown in the corresponding dQ/dV (Q represents charge capacity and V represents voltage) curves of Figs. 3(c) and 3(d), although the reduction peaks of both cells at around 3.0 V gradually shift to lower voltages as the cycle progresses, the voltage drop of LMNCO/Li cell (ΔV = 0.61 V) is higher than that of LMNCO-M@SNCN/Li cell (ΔV = 0.46 V) after 200 cycles. It indicates that LMNCO has undergone an irreversible phase transition from layered to spinel structure [28]. Moreover, we tested the cycling performance of cells at a high temperature of 55 °C with the rate of 1 C (Fig. S4(b) in the ESM). Obviously, LMNCO-M@SNCN/Li cell has better cycling stability with a capacity retention of 76.3% after 150 cycles, which is significantly higher than that of 42.1% for LMNCO/Li cell. In addition, the rate performance of Fig. 3(e) further highlights the excellent electrochemical performance of LMNCO-M@SNCN/Li cell. The discharge capacity of LMNCO-M@SNCN/Li cell is 161.0 mAh·g^{-1} at 5 C, with the capacity retention of 73.6% compared with 0.2 C, which is much higher than the 139.2 mAh·g^{-1} and 64.5% of LMNCO/Li cell, respectively.

To demonstrate the superiority of our work, we compared the cycling performance of triply modified Li-rich materials with those reported in earlier literatures [29–36] (Fig. 3(f)). It can be seen that the as-synthesized LMNCO-M@SNCN has the best cycling stability. Besides, to present the data visually, electrochemical performances were compared in the form of radar image in multiple directions (Fig. 3(g)). The results confirm that LMNCO-M@SNCN has better cycling stability and discharge capacity in various application scenarios, especially under harsh conditions.

To elucidate the mechanism of the enhanced electrochemical performance of LMNCO-M@SNCN, we investigated the kinetic properties of electron and ion transport for both samples. Firstly, the electron work function (Φ_c) of LMNCO and LMNCO-M@SNCN was analyzed using the Kelvin probe force microscopy (KPFM) model of AFM. The Φ_c describes the difference between the vacuum energy level (E_v) and the Fermi energy level (E_f), and the smaller the value of Φ_c, the more susceptible the materials are to escape of electrons. The three-dimensional morphology of the measured area is given in Figs. S5(a) and S5(b) in the ESM, and the height difference between the two samples is basically equal. The corresponding potential distributions of the two samples are shown in Figs. 4(a) and 4(b). Subsequent statistical digitization of the potential distribution (Fig. 4(c)) reveals that the signal peak of Φ_c for LMNCO-M@SNCN at 3.82 eV is lower than that of LMNCO at 3.95 eV. It indicates a faster electron transfer kinetics among the active materials in LMNCO-M@SNCN, which is conducive to improving the rate performance of the electrodes and alleviating polarization. In addition, we have conducted conductivity tests on two samples using the four-probe technique, and the results also confirm that the electronic conductivity of LMNCO-M@SNCN is significantly improved (Fig. S5(c) in the ESM). To elucidate the enhancement mechanism of the LMNCO-M@SNCN electron transport rate, we analyzed the electronic structures of the two samples using density of states (DOS) calculations in DFT theory (Figs. 4(d) and 4(e)). Compared with LMNCO, the C increases the density of electronic states in the conduction band region near the Fermi level of LMNCO-M@SNCN, and the energy band gap reduces from the pristine 0.46 to 0.13 eV, indicating that LMNCO-M@SNCN has higher electron conductivity. This is consistent with the results of KPFM and four-probe tests. Besides, the Li^+ diffusion coefficients (D_{Li^+}) of the two samples were calculated by the GITT technique, as shown in Fig. 4(f). It is obvious that the average D_{Li^+} of LMNCO-M@SNCN is 6.9108 × 10^{-11} cm^2·s^{-1}, which is about twice as much as the 3.8326 × 10^{-11} cm^2·s^{-1} of LMNCO in the lithiation stage. Therefore, for LMNCO-M@SNCN, the SNCN provides additional electrons to the conduction band, thus effectively increasing the electron transfer rate among the active materials. Meanwhile, the synergy of Mo^{6+} doping and OVs fabrication broadens and stabilizes the Li^+ diffusion channel,

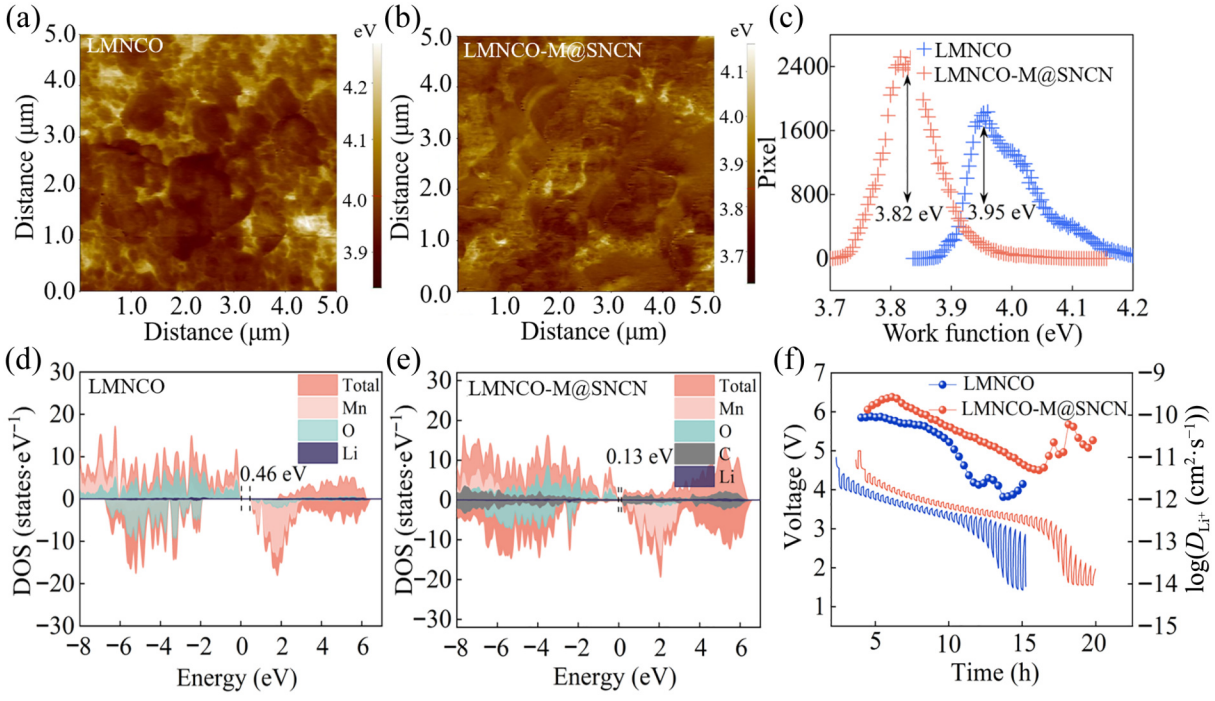

Figure 4 ((a) and (b)) The potential distribution, (c) the normal distribution of work function, and ((d) and (e)) the DOS images of LMNCO and LMNCO-M@SNCN. (f) GITT curves and the corresponding log D_{Li^+} of LMNCO and LMNCO-M@SNCN.

improving the kinetic properties of Li^+. That is, LMNCO-M@SNCN achieves simultaneous improvement in ionic and electronic conductivity, thus significantly enhancing the rate performance.

To reveal the synergistic effect of bulk Mo doping, surface OVs defects, and SNCN coating on the structural stability of the materials, the *in-situ* electrochemical XRD was performed to analyze the reversibility of the structural evolution during the initial cycling. As shown in Figs. 5(a) and 5(b), the intensity of the red color reflects the intensity change of (003), (104), and (108)/(110) diffraction peaks. Among them, the obvious (108)/(110) splitting peaks of the two samples indicate that the layered structure of the materials remains intact during the charge–discharge process. The (003) peaks of LMNCO and LMNCO-M@SNCN shift toward lower angle during charging, which is attributed to the enhanced electrostatic repulsion between adjacent oxygen layers during delithiation, resulting in increased interlayer spacing. During the subsequent discharge process, the (003) peak progressively returns to its initial position, indicating the reversible intercalation of Li^+ into the crystal lattice. After ending the cycle, the (003) peak of LMNCO-M@SNCN exhibits merely a 0.05° shift from its initial position, significantly lower than the 0.12° shift observed in pristine LMNCO. This result demonstrates that the triple-modification strategy synergistically enhances the structural reversibility of LMNCO-M@SNCN, thereby establishing durable and stable transport pathways for Li^+ diffusion. Similar trends are also observed for (104) peak, and the (104) peak of LMNCO-M@SNCN is almost restored to the initial position, confirming the excellent structural stability and reversibility of the modified LMNCO-M@SNCN. This result is further confirmed by the position change of (003) peak in XRD patterns before and after cycles (Fig. S6 in the ESM). That is, the (003) diffraction peak of LMNCO-M@SNCN remains nearly unchanged after 200 cycles, whereas the (003) peak of pristine LMNCO shifts to a lower angle by 0.3°.

To systematically evaluate the ability of the LMNCO-M@SNCN to resist electrolyte erosion, we analyzed the chemical composition of the surface of two samples after 200 cycles using XPS. In the F 1s spectra of Fig. 6(a), the characteristic peaks at 684.5 and 687.3 eV are attributed to LiF and $-CF_2-$ species, respectively [37]. The peak intensity of LiF in LMNCO-M@SNCN is significantly weaker compared to that in LMNCO, which means a lighter degree of surface side reactions in LMNCO-M@SNCN. The regeneration of LiF is associated with the attack of the by-product HF on the cathode material, which not only consumes the active lithium but also inhibits the electron transfer among particles, thereby accelerating the capacity decay of the electrode [38]. Besides, as shown in the P 2p spectra of Fig. 6(b), the characteristic peak at 134.7 eV corresponds to the $Li_xPO_yF_z$ species, which mainly originates from the decomposition of the lithium salt $LiPF_6$ and its subsequent combination with active Li^+ [39]. Obviously, the relative content of $Li_xPO_yF_z$ species on the LMNCO-M@SNCN surface is slightly lower than that on the LMNCO surface, further indicating that LMNCO-M@SNCN suppresses side reactions at the electrode–electrolyte interface. As shown in the O 1s spectra of Fig. 6(c),

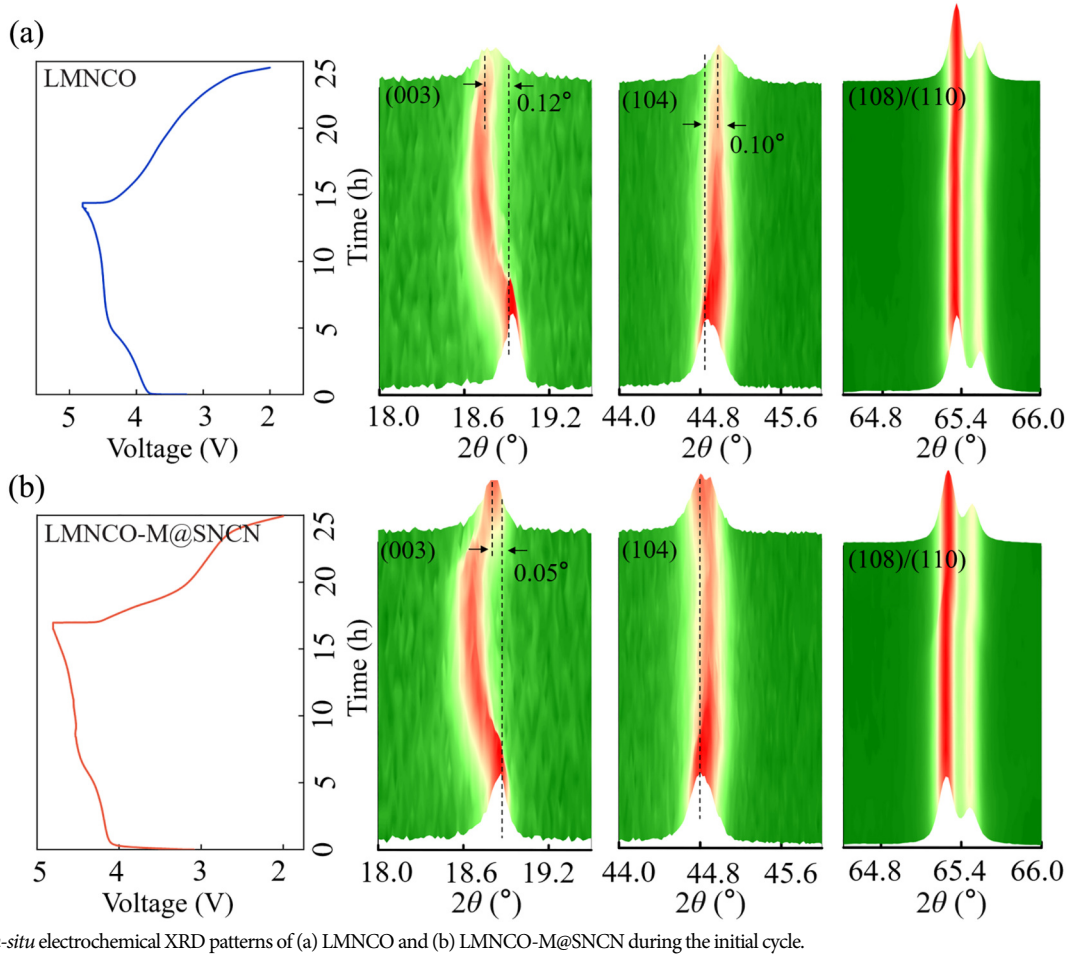

Figure 5 The *in-situ* electrochemical XRD patterns of (a) LMNCO and (b) LMNCO-M@SNCN during the initial cycle.

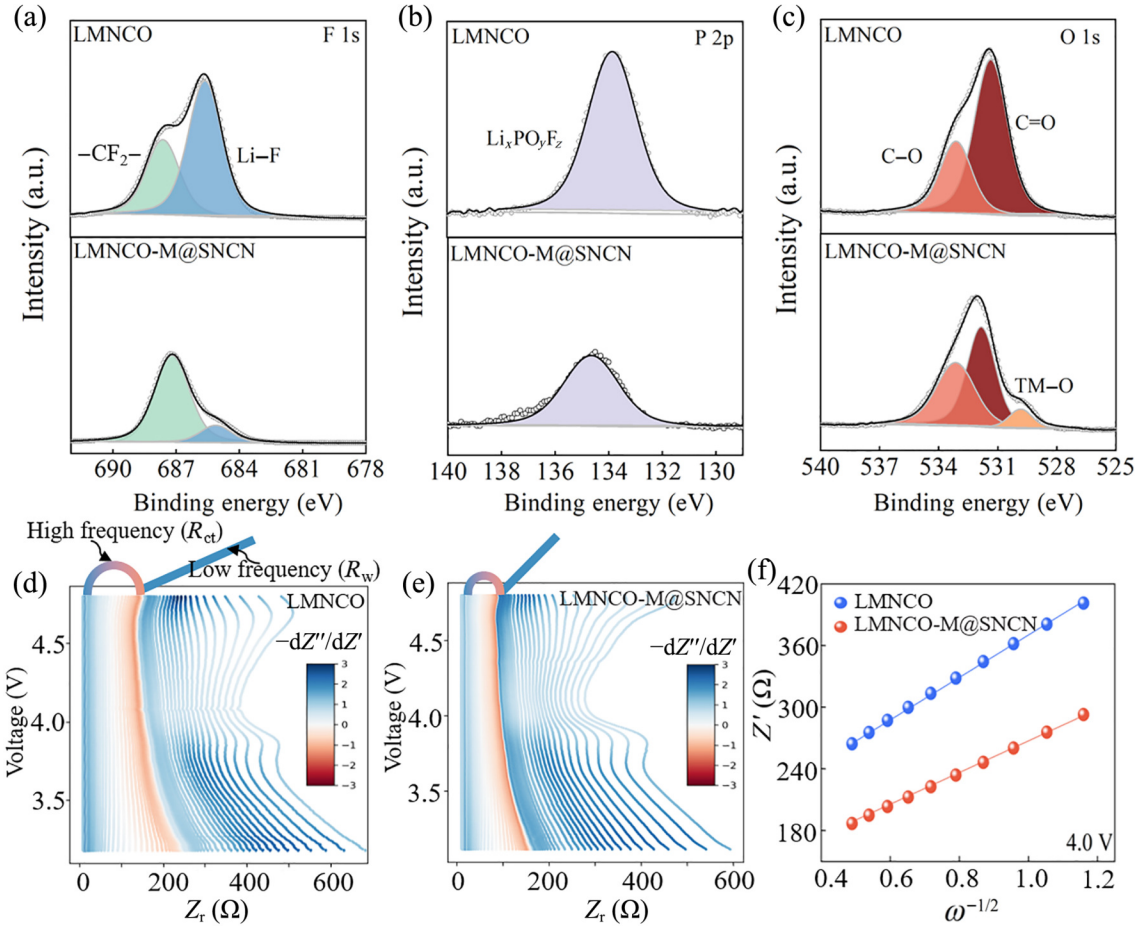

Figure 6 ((a)–(c)) XPS spectra of (a) F 1s, (b) P 2p, and (c) O 1s for the LMNCO and LMNCO-M@SNCN after 200 cycles. ((d) and (e)) The PRIs-EIS images for (d) LMNCO/Li and (e) LMNCO-M@SNCN/Li during the 200th charging process. (f) The curves of $\omega^{-1/2}$–Z' relation of LMNCO and LMNCO-M@SNCN at 4.0 V.

the organic C=O (531.5 eV) and the C–O (533.2 eV) species are present in both samples, whereas the characteristic peak located at 529.5 eV belonging to the TM–O species is found only in LMNCO-M@SNCN. It indicates that SNCN coating effectively resists electrolyte corrosion and TM dissolution, significantly stabilizing the surface structure of the modified cathode. Moreover, the whole evolution of kinetic properties during the 200th charging process was further analyzed by PRIs-EIS technique. As shown in Figs. 6(d) and 6(e), multiple data points obtained at the same frequency under different potentials form a cluster of equifrequent curves. In these curves, the horizontal color gradient band from blue to red represents a time constant in the traditional Nyquist curve (−dZ″/dZ'), in which the high frequency range corresponds to the charge transfer resistance (R_{ct}) and the low frequency range corresponds to the Li^+ ion diffusion resistance in the cathode (Warburg impedance, R_w) [40, 41]. The impedances of both samples show a similar changing trend in the voltage range of 3.0–4.8 V. Notably, the R_{ct} of LMNCO-M@SNCN is significantly lower than that of LMNCO during the delithiation process, mainly attributed to the decrease of inorganic products LiF and $Li_xPO_yF_z$ on the LMNCO-M@SNCN surface, as well as the enhancement of surface conductivity. Subsequently, based on the relationship between the Z' and the inverse square root of the angular frequency ($\omega^{-1/2}$) in the low frequency region, the D_{Li^+} of the two samples was calculated at 4.0 V (Fig. 6(f)). The calculation results showed that the D_{Li^+} of LMNCO-M@SNCN is significantly enhanced to 9.06×10^{-14} compared to LMNCO ($D_{Li^+} = 5.37 \times 10^{-14}$ $cm^2 \cdot s^{-1}$). This enhancement confirms that the triple modification strategy effectively strengthens the structural stability of material, enabling LMNCO-M@SNCN to maintain excellent Li^+ transport kinetics during prolonged cycling.

The morphologies of LMNCO and LMNCO-M@SNCN after 200 cycles at 1 C were directly analyzed by SEM and HRTEM. As shown in the SEM of Fig. 7(a), the secondary particles of LMNCO show a large amount of cracking and pulverization, attributed to the conformational collapse caused by inhomogeneous internal stresses and external influences. Different from that, the integrity of the LMNCO-M@SNCN particles is well maintained, and no visible cracks appeared (Fig. 7(b)), confirming their excellent mechanical stability. The enhancement of LMNCO-M@SNCN mechanical properties and resistance to electrolyte corrosion significantly inhibited TM dissolution. As shown in the ICP-OES result (Fig. 7(c)), the concentration of Ni, Co, and Mn deposited on the Li anode surface for LMNCO-M@SNCN/Li cell is almost reduced to about 1/3 of that for LMNCO/Li cell. Besides, Figs. 7(d) and 7(e) show the HRTEM images of LMNCO and LMNCO-M@SNCN, respectively. It can be observed that LMNCO undergoes a severe phase transition after cycling. This is, as the cycle progresses, the pristine layered structure disappears, and the proportion of rock salt phase structure increases significantly. The deterioration of the phase transition means that the Li^+ diffusion path is blocked, resulting in severe capacity/voltage decay. For LMNCO-M@SNCN,

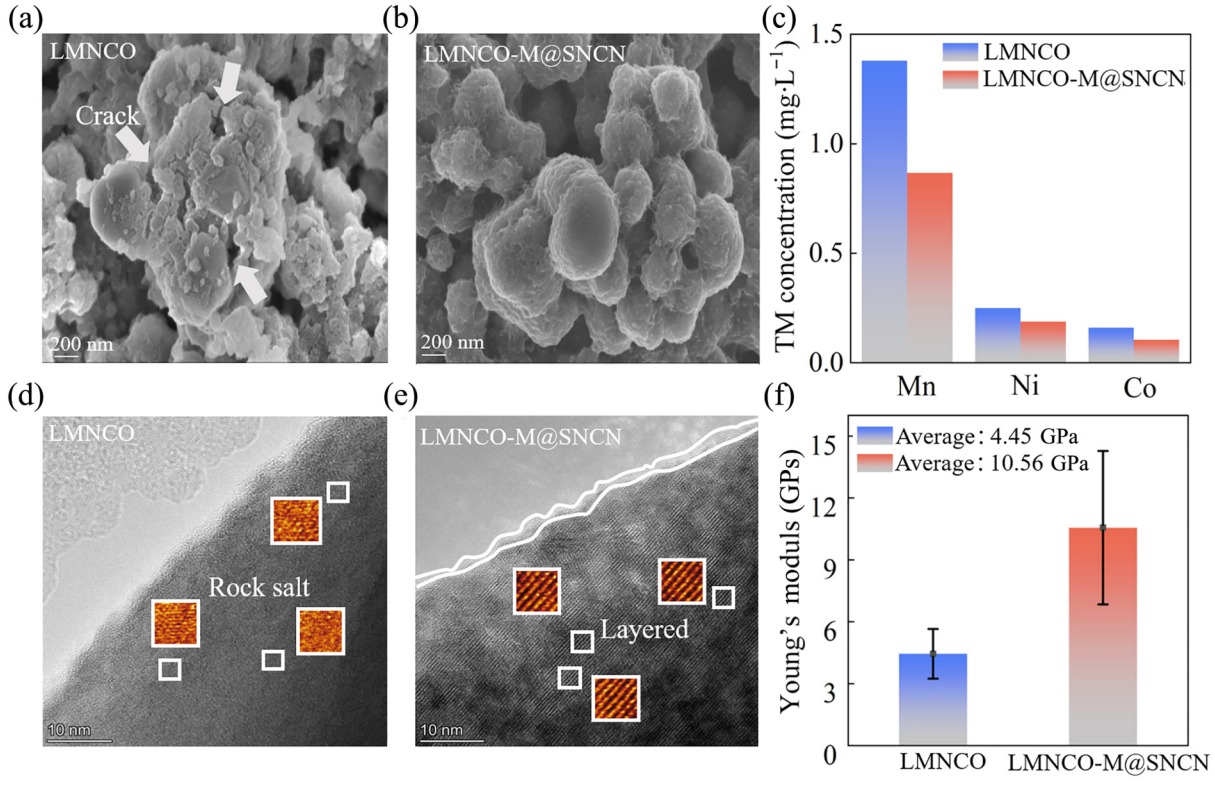

Figure 7 ((a) and (b)) SEM images, (c) TM concentration deposited on anode surface, ((d) and (e)) TEM images, and (f) the Young's modulus for LMNCO and LMNCO-M@SNCN after 200 cycles at 1 C.

there are ordered lattice stripes and layered structures on both the surface and the bulk, indicating that the phase transition has been effectively mitigated. In addition, the Young's modulus of both samples after cycling was determined using the Derjaguin–Muller–Toporov (DMT) mode of the AFM. Figure S7 in the ESM shows the morphology of the average Young's modulus of the collected LMNCO-M@SNCN and LMNCO. As shown in (Fig. 7(f)), the average Young's modulus of LMNCO-M@SNCN after 200 cycles is as high as 10.56 GPa, much higher than that of LMNCO (4.45 GPa), indicating that the enhancement of surface and bulk structure stability can significantly improve the mechanical strength of LMNCO-M@SNCN, thereby effectively inhibiting particle cracking and TM dissolution.

Combining all the results above, the mechanism of the triple modification engineering of bulk Mo^{6+} doping, surface OVs construction and SNCN coating to enhance the electrochemical performance of LMNCO-M@SNCN is shown in Fig. 8. As the control sample, pristine LMNCO is prone to cause the TMs out-of-plane migration, TM/O loss and severe side reactions during cycling, which will deteriorate the surface and bulk structure of materials. Subsequently, it leads to irreversible phase transitions and crack formation, interrupting the electrons and Li^+ transport among particles and resulting in a rapid capacity decay. For the LMNCO-M@SNCN, Mo^{6+} and OVs strengthen the crystal structure by inhibiting oxygen loss and TM migration, and SNCN resists corrosion of the material surface by the electrolyte while

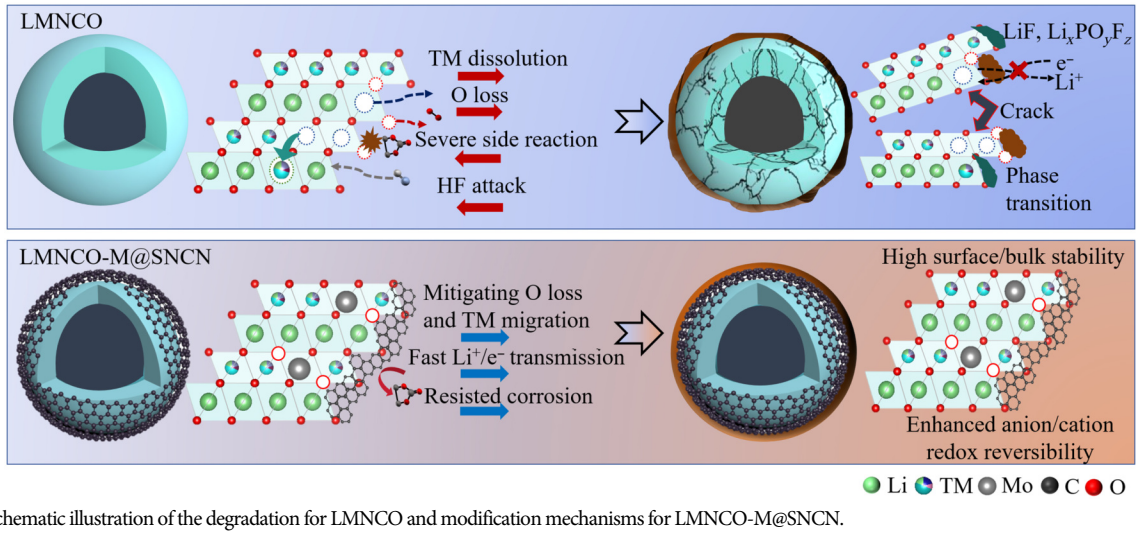

Figure 8 Schematic illustration of the degradation for LMNCO and modification mechanisms for LMNCO-M@SNCN.

maintaining high conductivity. The synergistic effect of the triple modification accelerates the fast electron and Li^+ transport, enhances the reaction reversibility of anions and cations, and strengthens the structural stability of the material from the surface to the bulk, ultimately resulting in excellent electrochemical performance of LMNCO-M@SNCN in multiple application scenarios.

4 Conclusions

In summary, bulk Mo^{6+} doping, OVs defects, and SNCN surface coating were successfully constructed in LMNCO-M@SNCN. The SNCN provides additional electrons for the LMNCO in the conduction band region, while Mo^{6+} doping and OVs defects broaden and stabilize the Li^+ diffusion channel, achieving simultaneous improvement in ionic and electronic conductivity. Mo^{6+} and OVs mitigate the irreversible phase transitions caused by oxygen loss and TM out-of-plane migration, significantly improving the structural reversibility of LMNCO-M@SNCN. Meanwhile, SNCN inhibits the corrosion of the material surface by the electrolyte while maintaining high conductivity. Under the effect of triply synergistic modification, the LMNCO-M@SNCN layered structure remains intact even after undergoing many times of lithiation/delithiation. As a result, LMNCO-M@SNCN shows more excellent cycle life and discharge capacity compared with those reported in earlier literatures, with the capacity retention is 94.6% after 200 cycles at 1 C, and a high rate capacity of 161.0 $mAh{\cdot}g^{-1}$ at 5 C. Especially, under harsh conditions, the capacity retention is 76.3% after 150 cycles at 55 ℃ with 1 C. This work provides a new solution for developing advanced LMNCO cathode materials.

Electronic Supplementary Material: Supplementary material (Figs. S1–S7 and Table S1) is available in the online version of this article at https://doi.org/10.26599/NR.2025.94907813.

Data availability

All data needed to support the conclusions in the paper are presented in the manuscript and the Electronic Supplementary Material. Additional data related to this paper may be requested from the corresponding author upon request.

Acknowledgements

This work was supported by Key Research and Development Program of Gansu (No. 24YFGA025), Joint Research Foundation of Gansu (No. 21JRRA832), the National Natural Science Foundation of China (No. 22269012), and Gansu Provincial Department of Education: Graduate Student "Innovation Star" Project (No. 2025CXZX532).

Declaration of competing interest

All the contributing authors report no conflict of interests in this work.

Author contribution statement

X. P. C. was involved in conceptualization; data curation; formal analysis; investigation; methodology; project administration; writing – original draft; and writing – review & editing. S. Y. L. was involved in funding acquisition and project administration. N. S. Z. was involved in software and supervision. J. W. Z. was involved in software. J. X. Y. was involved in administration and investigation. X. L. C. was involved in visualization and writing – review & editing. All the authors have approved the final manuscript.

Use of AI statement

None.

References

[1] Xu, J. J.; Cai, X. Y.; Cai, S. M.; Shao, Y. X.; Hu, C.; Lu, S. R.; Ding, S. J. High-energy lithium-ion batteries: Recent progress and a promising future in applications. *Energy Environ. Mater.* **2023**, *6*, e12450.

[2] Xiao, J.; Shi, F. F.; Glossmann, T.; Burnett, C.; Liu, Z. From laboratory innovations to materials manufacturing for lithium-based batteries. *Nat. Energy* **2023**, *8*, 329–339.

[3] He, W.; Guo, W. B.; Wu, H. L.; Lin, L.; Liu, Q.; Han, X.; Xie, Q. S.; Liu, P. F.; Zheng, H. F.; Wang, L. S. et al. Challenges and recent advances in high capacity Li-rich cathode materials for high energy density lithium-ion batteries. *Adv. Mater.* **2021**, *33*, 2005937.

[4] Li, Q. Y.; Ning, D.; Wong, D.; An, K.; Tang, Y. X.; Zhou, D.; Schuck, G.; Chen, Z. H.; Zhang, N.; Liu, X. F. Improving the oxygen redox reversibility of Li-rich battery cathode materials via Coulombic repulsive interactions strategy. *Nat. Commun.* **2022**, *13*, 1123.

[5] Guo, W. B.; Zhang, C. Y.; Zhang, Y. G.; Lin, L.; He, W.; Xie, Q. S.; Sa, B.; Wang, L. S.; Peng, D. L. A universal strategy toward the precise regulation of initial Coulombic efficiency of Li-rich Mn-based cathode materials. *Adv. Mater.* **2021**, *33*, 2103173.

[6] Zheng, H. F.; Han, X.; Guo, W. B.; Lin, L.; Xie, Q. S.; Liu, P. F.; He, W.; Wang, L. S.; Peng, D. L. Recent developments and challenges of Li-rich Mn-based cathode materials for high-energy lithium-ion batteries. *Mater. Today Energy* **2020**, *18*, 100518.

[7] Liu, T. C.; Liu, J. J.; Li, L. X.; Yu, L.; Diao, J. C.; Zhou, T.; Li, S. N.; Dai, A.; Zhao, W. G.; Xu, S. Y. et al. Origin of structural degradation in Li-rich layered oxide cathode. *Nature* **2022**, *606*, 305–312.

[8] Jin, Y. L.; Zhao, Z. R.; Ren, P. G.; Zhang, B. F.; Chen, Z. Y.; Guo, Z. Z.; Ren, F.; Sun, Z. F.; Liu, S. H.; Song, P. et al. Recent advances in oxygen redox activity of lithium-rich manganese-based layered oxides cathode materials: Mechanism, challenges and strategies. *Adv. Energy Mater.* **2024**, *14*, 2402061.

[9] Cao, B.; Li, T. Y.; Zhao, W. G.; Yin, L.; Cao, H. B.; Chen, D.; Li, L. X.; Pan, F.; Zhang, M. J. Correlating rate-dependent transition metal dissolution between structure degradation in Li-rich layered oxides. *Small* **2023**, *19*, 2301834.

[10] Zhao, J. T.; Zhang, X.; Liang, Y.; Han, Z. J.; Liu, S. Q.; Chu, W. Q.; Yu, H. J. Interphase engineering by electrolyte additives for lithium-rich layered oxides: Advances and perspectives. *ACS Energy Lett.* **2021**, *6*, 2552–2564.

[11] Mao, D. D.; Fan, Z. W.; Song, L. T.; Zhang, P.; Xie, J. P.; Su, S.; Liu, G. Y.; Wang, H. F.; Chu, W. G. Effective regulation of Li_2MnO_3-like single-component in high-nickel Li-rich layered oxides by trace Sb doping for remarkable performance improvement. *Nano Energy* **2024**, *121*, 109231.

[12] Cai, X. P.; Zhang, N. S.; Ding, H.; Zhao, D. N.; Zhou, J. F.; Zhang, J. W.; Song, L. H.; Huang, J.; Li, C. L.; Li, S. Y. Understanding the mechanism of performance difference when substituting Al for different transition metal ions in Li-rich Mn-based cathode materials. *Acta Mater.* **2023**, *258*, 119220.

[13] Shin, Y.; Kan, W. H.; Aykol, M.; Papp, J. K.; McCloskey, B. D.; Chen, G. Y.; Persson, K. A. Alleviating oxygen evolution from Li-excess oxide materials through theory-guided surface protection. *Nat. Commun.* **2018**, *9*, 4597.

[14] Dong, S. D.; Zhou, Y.; Hai, C. X.; Zeng, J. B.; Sun, Y. X.; Shen, Y.; Li, X.; Ren, X. F.; Sun, C.; Zhang, G. T. et al. Understanding electrochemical performance improvement with Nb doping in lithium-rich manganese-based cathode materials. *J. Power Sources* **2020**, *462*, 228185.

[15] Wang, G.; Xie, C. H.; Wang, H.; Li, Q.; Xia, F. J.; Zeng, W. H.; Peng, H. Y.; van Tendeloo, G.; Tan, G. J.; Tian, J. S. et al. Mitigated oxygen loss in lithium-rich manganese-based cathode enabled by strong Zr–O affinity. *Adv. Funct. Mater.* **2024**, *34*, 2313672.

[16] Cai, X. P.; Li, S. Y.; Zhang, N. S.; Zhang, J. W.; Yan, J. X.; Gao, C. K.; Cui, X. L. Trace Mo doping-derived symbiotic structure to improve the stability of lithium-rich manganese-based cathode. *Chem. Eng. J.* **2025**, *517*, 164410.

[17] Li, Y.; Shi, Z. P.; Qiu, B.; Zhao, J. L.; Li, X.; Zhang, Y. B.; Li, T. T.; Gu, Q. W.; Gao, J.; Liu, Z. P. Optimizing both bulk and surface structure of Li-rich layered cathodes for long-life and safe Li-ion batteries. *Adv. Funct. Mater.* **2023**, *33*, 2302236.

[18] Jiang, Q. T.; Li, X. F.; Hao, Y. C.; Zuo, J. X.; Duan, R. X.; Li, J.; Cao, G. Q.; Wang, J. J.; Wang, J.; Li, M. et al. Oxygen-vacancy-assisted dual functional surface coatings suppressing irreversible phase transition of Li-rich layered oxide cathodes. *Adv. Funct. Mater.* **2025**, *35*, 2400670.

[19] Li, Z.; Cao, S.; Chen, J. R.; Wu, L.; Chen, M. F.; Ding, H.; Wang, R. J.; Guo, W.; Bai, Y. S.; Liu, M. et al. Modulating surface architecture and electronic conductivity of Li-rich manganese-based cathode. *Small* **2024**, *20*, 2400641.

[20] Zhao, J. Y.; Su, Y. F.; Dong, J. Y.; Hao, J. N.; Che, H. Q.; Lu, Y.; Li, N.; Zhang, B.; Zhang, P.; Wu, F. et al. Boosting reaction homogeneity through reverse gradient fluorination for high-performance Li-rich layered cathodes. *Energy Stor. Mater.* **2025**, *76*, 104137.

[21] Li, S. Y.; Fu, X. L.; Liang, Y. W.; Wang, S. X.; Zhou, X.; Dong, H.; Tuo, K.; Gao, C. K.; Cui, X. L. Enhanced structural stability of boron-doped layered@spinel@carbon heterostructured lithium-rich manganese-based cathode materials. *ACS Sustainable Chem. Eng.* **2020**, *8*, 9311–9324.

[22] Cheng, Y. X.; Wu, Z.; Dai, X.; Hu, J. X.; Tai, Z. G.; Sun, J. J.; Liu, Y.; Tan, Q.; Liu, Y. N. Enhanced electrochemical properties of potassium-doped lithium-rich oxide@carbon as cathode material for lithium-ion batteries. *J. Colloid Interface Sci.* **2022**, *605*, 718–726.

[23] Sun, G. X.; Zhu, B.; He, R.; Liang, Q. D.; Jiang, S. Y.; Ren, Y.; Pan, X. X.; Sun, Y. Q.; Lu, M.; Zhang, W. X. et al. Synergy of F^- doping and fluorocarbon coating on elevating high-voltage cycling stability of NCM811 for lithium-ion batteries. *Rare Met.* **2025**, *44*, 1577–1593.

[24] Li, S. C.; Liu, Y. Y.; Zhang, Y. G.; Gao, G. Y.; Guo, W. B.; Xu, Q. X.; Wu, H. L.; Fan, M. J.; Wang, L. S.; Sa, B. S. et al. Multi-functionalized full-interface integrated engineering towards highly reversible Li-rich Mn-based cathode. *Energy Stor. Mater.* **2024**, *66*, 103241.

[25] Guo, J. L.; Lai, Y. Q.; Gao, X. G.; Li, S. H.; Zhang, H. Y.; Guan, C. H.; Chen, L.; Yang, Z. D.; Li, S. M.; Zhang, Z. A. Triggering cationic/anionic hybrid redox stabilizes high-temperature Li-rich cathodes materials via three-in-one strategy. *Energy Stor. Mater.* **2024**, *69*, 103383.

[26] Fang, Y. Y.; Su, Y. F.; Dong, J. Y.; Zhao, J. Y.; Wang, H. Y.; Li, N.; Lu, Y.; Wu, Y. J; Li, W. B.; Yang, N. et al. Ionic-electronic dual-conductor interface engineering and architecture design in layered lithium-rich manganese-based oxides. *Carbon Energy* **2025**, *7*, e642.

[27] Gao, X. G.; Zhang, H. Y.; Li, S. H.; Zhang, S.; Guan, C. H.; Hu, X. P.; Guo, J. L.; Lai, Y. Q.; Zhang, Z. A. Local electronic structure modulation enables fast-charging capability for Li-rich Mn-based oxides cathodes with reversible anionic redox activity. *Adv. Funct. Mater.* **2023**, *33*, 2304065.

[28] Liu, H.; Hua, W. B.; Kunz, S.; Bianchini, M.; Li, H.; Peng, J. L.; Lin, J.; Dolotko, O.; Bergfeldt, T.; Wang, K. et al. Tailoring superstructure units for improved oxygen redox activity in Li-rich layered oxide battery's positive electrodes. *Nat. Commun.* **2024**, *15*, 9981.

[29] Yang, F.; Li, Y. L.; Wang, Z.; Chen, C. G.; Guo, Z. M. Preparation and coating modification of lithium-rich layered oxides $Li_{1.2}Mn_{0.54}Ni_{0.13}Co_{0.13}O_2$ via Al_2O_3. *J. Appl. Electrochem.* **2023**, *53*, 1–8.

[30] Kang, S. W.; Wei, X. B.; Chu, Y. Q.; Mu, Y. B.; Zou, L. F.; Xu, X. Q.; Zhang, Q.; Zeng, L. Simultaneous dual modification of Li-rich Mn-based cathode in restraining oxygen release and structure distortion. *J. Mater. Chem. A* **2024**, *12*, 9584–9593.

[31] Zhao, E. Y.; Liu, X. F.; Hu, Z. B.; Sun, L. M.; Xiao, X. L. Facile synthesis and enhanced electrochemical performances of Li_2TiO_3-coated lithium-rich layered $Li_{1.13}Ni_{0.30}Mn_{0.57}O_2$ cathode materials for lithium-ion batteries. *J. Power Sources* **2015**, *294*, 141–149.

[32] Zhang, X. H.; Xie, X.; Yu, R. Z.; Zhou, J. R.; Huang, Y.; Cao, S.; Wang, Y.; Tang, K.; Wu, C.; Wang, X. Y. Improvement of the cycling stability of Li-rich layered Mn-based oxide cathodes modified by nanoscale $LaPO_4$ coating. *ACS Appl. Energy Mater.* **2019**, *2*, 3532–3541.

[33] Liu, F.; Sun, K. L.; Wei, T. Y.; Li, Z. H.; Ma, Z. Y.; Ding, Y. H.; Lei, G. T. Synergistic effect of interlayered doping and surface modification to improve the performance of Li-rich manganese-based cathode materials. *J. Alloy. Compd.* **2024**, *994*, 174759.

[34] Wang, T. T.; Zeng, W. H.; Zhu, J. W.; Tian, W. X.; Wang, J.; Tian, J. S.; Yuan, D. C.; Zhang, S. J.; Mu, S. C. SeO_2-infused grain boundaries effectively improve rate and stability performance of Li-rich manganese-based layered cathode materials. *Nano Energy* **2023**, *113*, 108577.

[35] Tai, Z. G.; Zhu, W.; Shi, M.; Xin, Y. F.; Guo, S. W.; Wu, Y. F.; Chen, Y. Z.; Liu, Y. N. Improving electrochemical performances of lithium-rich oxide by cooperatively doping Cr and coating Li_3PO_4 as cathode material for lithium-ion batteries. *J. Colloid Interface Sci.* **2020**, *576*, 468–475.

[36] Ji, X. Q.; Xu, Y. X.; Feng, H. L.; Wang, P. F.; Zhou, Y. C.; Song, J. C.; Xia, Q.; Tan, Q. Q. Surface $LiMn_{1.4}Ni_{0.5}Mo_{0.1}O_4$ coating and bulk Mo doping of Li-rich Mn-based $Li_{1.2}Mn_{0.54}Ni_{0.13}Co_{0.13}O_2$ cathode with enhanced electrochemical performance for lithium-ion batteries. *ACS Appl. Mater. Interfaces* **2021**, *13*, 47659–47670.

[37] Bai, P. X.; Ji, X.; Zhang, J. X.; Zhang, W. R.; Hou, S.; Su, H.; Li, M. J.; Deng, T.; Cao, L. S.; Liu, S. F. et al. Formation of LiF-rich cathode-electrolyte interphase by electrolyte reduction. *Angew. Chem., Int. Edit.* **2022**, *61*, e202202731.

[38] Fan, X. M.; Ou, X.; Zhao, W. G.; Liu, Y.; Zhang, B.; Zhang, J. F.; Zou, L. F.; Seidl, L.; Li, Y. Z.; Hu, G. R. et al. *In situ* inorganic conductive network formation in high-voltage single-crystal Ni-rich cathodes. *Nat. Commun.* **2021**, *12*, 5320.

[39] Wang, P.; Yan, D.; Wang, C. Y.; Ding, H.; Dong, H.; Wang, J.; Wu, S. M.; Cui, X. L.; Li, C. L.; Zhao, D. N. et al. Study of the formation and evolution of solid electrolyte interface via *in-situ* electrochemical impedance spectroscopy. *Appl. Surf. Sci.* **2022**, *596*, 153572.

[40] Cai, X. P.; Li, S. Y.; Zhou, J. F.; Zhang, J. W.; Zhang, N. S.; Cui, X. L. Mitigating chain degradation of lithium-rich manganese-based cathode material by surface engineering. *Energy Stor. Mater.* **2024**, *71*, 103624.

[41] Li, S. Y.; Li, J. N.; Wang, P.; Ding, H.; Zhou, J. F.; Li, C. Y.; Cui, X. L. Interface engineering regulation by improving self-decomposition of lithium salt-type additive using ultrasound. *Adv. Funct. Mater.* **2024**, *34*, 2307180.